Hindawi
Advances in Civil Engineering
Volume 2022, Article ID 8748109, 16 pages
https://doi.org/10.1155/2022/8748109

*Research Article*

# Effect of Wetting and Drying Cycles on the Dynamic Properties of Compacted Loess

**Jian Wang,[1] Mi-Jun Zhao,[1] Jun-Zheng Zhang,[1] Yan-Zhou Hao ,[2] and Rui-Xia He[2]**

[1]*Henan Bureau Group Co. Ltd of China Chemical and Geology, Zhengzhou, Henan 450000, China*
[2]*School of Civil and Transportation Engineering, Henan University of Urban Construction, Pingdingshan, Henan 467036, China*

Correspondence should be addressed to Yan-Zhou Hao; 30010508@hncj.edu.cn

Received 3 July 2022; Revised 27 October 2022; Accepted 3 November 2022; Published 14 November 2022

Academic Editor: Wayne Yu Wang



This paper investigates the dynamic properties of compacted loess under wetting and drying (*W-D*) cycles. A series of tests were conducted on compacted loess samples, namely, the soil dynamic triaxial test and the scanning electron microscopy (SEM) test. The test results showed that the dynamic stress-strain relationship of the compacted loess under the action of *W-D* cycles accords with the Hardin–Drnevich model. The initial dynamic shear modulus ($G_0$) and the maximum dynamic shear stress ($\tau_y$) of the compacted loess first decreased and then increased with the number of *W-D* cycles ($n$) increasing. The damping ratio ($\lambda$) increased linearly with the dynamic strain ($\varepsilon_d$) increasing in the semilogarithmic coordinate. The defined change rate of the damping ratio ($\eta$) first increased and then decreased with the $n$ increasing. The macrostructure and microstructure characteristics of samples in the process of *W-D* cycles indicate that the increasing number of pores in the humidifying process and the cracks on the surface and inside of samples during dehumidification lead to the structural damage and dynamic properties reduction of compacted loess. The main reasons for structure strengthening and dynamic properties increasing are that soil particle structure develops to mosaic structure, pore structure develops to uniform small pore, and matrix suction makes soil sample tend to be dense.

## 1. Introduction

Loess is located in an area with frequent earthquakes having high intensity in China. The study on the dynamic properties of loess is significance to the earthquake prevention and disaster reduction of the filling foundation, subgrade, slope, and other projects in the loess area. Compaction is the main methods for the foundation treatment of fill engineering, which eliminated the collapsibility of loess [1–3].

The wetting and drying (*W-D*) cycles caused by the climate changes such as precipitation or evaporation and the rise or fall of groundwater level change the microstructure of the soil, made the strength deterioration of the soil mass [4–6]. The *W-D* cycles effected visible macroporosity and unresolved mesoporosity [7], made the different aggregate breakdown and to influence aggregate stability [8], and had a detrimental effect on the compressive strength of the soil samples ([9], Zhang et al. 2018).

Many studies focused on the static properties of compacted loess under the effects of *W-D* cycles. The *W-D* cycles have produced a degradation effect on the shear strength of undisturbed loess and compacted loess [10], Yuan et al. 2017. According to the degradation pattern of the static strength, a model of the degradation of the static strength was established, which was used to study the stability of the filled slope of compacted loess [11]. The *W-D* cycles have a significant effect on the triaxial shear properties of compacted loess, with the number of *W-D* cycles increasing, the stress-strain curve of compacted loess moves down sharply, then up gradually, and finally tends to be stable [12].

The dynamic stress-strain relationship of the saturated compacted loess conforms to the hyperbolic model, whereas the relationship among the initial dynamic shear modulus ($G_0$), the maximum dynamic stress, and the axial consolidation stress conforms to a power function [13, 14]. The dynamic elastic modulus ($E_d$) of compacted loess decreases

with the dynamic strain increasing and tends to stabilize gradually. Furthermore, the variation trend is basically the same under different dry densities, different moisture contents, and different confining pressures (Li et al., 2009). The initial dynamic shear modulus decreases with the water content increasing, while it increases with the dry density and confining pressure increasing [15]. The initial stress, middle principal stress coefficient, and the rotation of the principal stress axis have an obvious effect on the dynamic proprieties of compacted loess (Yang et al. 2010).

However, scholars pay little attention on the soil dynamic properties effect of *W-D* cycles. The dynamic strength of silty clay obviously increased after *W-D* cycles [16]. The dynamic strength of compacted loess decreased first and then increased gradually with the number of *W-D* cycles increasing [17]. The influence of *W-D* cycles is not considered in the study of dynamic properties of compacted loess.

After the completion of the filling project, the soil dynamic properties changed due to repeated *W-D* cycles such as rainfall, evaporation, and groundwater level rise and fall. However, there is no experimental study on the dynamic characteristics change of compacted loess after *W-D* cycles. In this paper, the dynamic properties of compacted loess after *W-D* cycles were tested and studied, and their variation rules were discussed.

The *W-D* cycles were carried out to simulate the impact of natural factors, such as rainfall, evaporation, rise of groundwater level, and the fall of groundwater level after the completion of the filling project. The dynamic stress-strain relationship, dynamic shear modulus, and damping ratio of compacted loess were investigated by dynamic triaxial tests with different *W-D* cyclic paths and different numbers of *W-D* cycles. The evolution of the microstructural mechanism of compacted loess was studied using a scanning electron microscope (SEM) under different *W-D* cycles numbers and paths.

## 2. Test Overview

*2.1. Sample Preparation.* The samples were $Q_3$ Malan loess in China. The physical properties are listed in Table 1. Loess samples from the soil layer were naturally air-dried and then pulverized using a rubber hammer, which separated the cemented particles only but did not damage the loess particles. The pulverized loess was sieved through a 2 mm mesh in order to prepare soil samples with a water content of 18.9%, which were sealed with plastic film for more than 48 hours to ensure the water content remains well-distributed and constant. The sample was put into the sample preparation device which was vertically compacted in four layers, the dry density was 1.70 g/cm$^3$ (the degree of compaction is 98.3%), and the diameter of the sample was 39.1 mm and the height was 80 mm, which was used for the dynamic triaxial test. The error was controlled to be ≤0.02 g/cm$^3$.

*2.2. W-D Cycle Process.* The initial moisture content was 18.9% for *W-D* cycles, and the saturated moisture content was 23%. According to the change process of soil moisture content, four kinds of *W-D* cycle paths were set, respectively: 18.9%-saturation- 8.9%, 18.9%–12.9%-saturation-12.9%, 18.9%–6.9%-saturation-6.9%, and 18.9%–0.9%-saturation-0.9%. The corresponding test numbers of the four *W-D* cycle paths were *a*, *b*, *c*, and *d*. The change amplitude of moisture content corresponding to the four *W-D* cycle paths was 4.1%, 10.1%, 16.1%, and 22.1%, respectively. The number of *W-D* cycles ($n$) was 0, 3, 6, 9, and 12, respectively, (Table 2).

The vacuum saturation method was used for sample saturation, whereas the degree of saturation was more than 98% for which the difference was not more than 0.1%. In the process of sample dehumidification, low temperature drying method (40°C) was adopted for *a*, *b*, and *c* paths, whereas the path of *d* was first dried at a low temperature (40°C) and then dried at a high temperature (105°C). After humidification or dehumidification, the samples were sealed with fresh-keeping film and placed in a moisturizing cylinder for more than 48 hours to ensure the water was distributed evenly. The moisture content of the loess sample was achieved by controlling its quality with an accuracy of ±0.1 g. In order to ensure that the samples were not affected by man-made damage during the *W-D* cycles, the samples were wrapped with plastic wrap and wrapped with tape after preparation (Figure 1), which was conducive to the migration of water in the soil through both ends of the sample, approximately simulating the one-dimensional migration of water.

After the *W-D* cycles reached the required number, the moisture content of the unified test was found to be 18.9%, which was conducive to the comparative analysis of the test data.

*2.3. Dynamic Triaxial Test.* The samples after the W-D cycles were used for a dynamic triaxial test to obtain dynamic characteristics. Dynamic triaxial test adopts the soil dynamic triaxial testing apparatus, which is produced by GDS, UK (Figure 1).

First, the sample was installed in the pressure chamber. After the pressure chamber was filled with water, the advanced loading module was used to load the sample step by step for drainage and consolidation. The consolidation ratio ($K$) is the ratio of axial pressure to confining pressure, which $K = 1.5$ in this paper. Consolidation confining pressure ($\sigma_c$) was loaded in four stages: 50 kPa, 100 kPa, 150 kPa, and 200 kPa. The corresponding axial biases were 25 kPa, 50 kPa, 75 kPa, and 100 kPa, respectively. The consolidation completion standard was that the axial deformation was less than 0.002 mm within 5 minutes.

The dynamic stress was applied to the specimen using the stress control loading mode. The dynamic triaxial test adopted the sine wave. The vibration frequency ($f$) is the number of vibration cycles per second, which $f = 1.0$ Hz in this paper. After consolidation, the drain valve was closed and the increment of the dynamic stress value of 10 kPa was a dynamic load to be applied on the sample for progressive cyclic loading (Table 3). The number of vibrations ($N$) for each level of dynamic stress was 10.

Table 1: The physical properties of loess.

| Relative density, GS | Optimal moisture content, w (%) | Maximum dry density, $\rho d$ (g/cm$^3$) | Plasticity index, $I_p$ | Particle composition (%) | | | |
|---|---|---|---|---|---|---|---|
| | | | | >0.075 mm | 0.075–0.01 mm | 0.01–0.005 mm | <0.005 mm |
| 2.72 | 18.9 | 1.73 | 12.2 | 3.72 | 52.18 | 15.44 | 28.66 |

Table 2: *W-D* cycle scheme of compacted loess.

| Test number | Dry density $\rho_d$ (g/cm$^3$) | Initial moisture content (%) | *W-D* cycle path | *W-D* cycle number *n* |
|---|---|---|---|---|
| *a* | 1.70 | 18.9 | 18.9%-saturation-18.9% | 0, 3, 6, 9, 12 |
| *b* | 1.70 | 18.9 | 18.9%-12.9%-saturation-12.9% | 0, 3, 6, 9, 12 |
| *c* | 1.70 | 18.9 | 18.9%-6.9%-saturation-6.9% | 0, 3, 6, 9, 12 |
| *d* | 1.70 | 18.9 | 18.9%-0.9%-saturation-0.9% | 0, 3, 6, 9, 12 |

Figure 1: Dynamic triaxial testing apparatus and some *W-D* cycle samples.

Table 3: The scheme of dynamic triaxial test.

| Test number | Vibration frequency *f* (Hz) | Consolidation ratio *K* | Consolidation confining pressure $\sigma_c$ (kPa) | Dynamic stress $\sigma_d$ (kPa) |
|---|---|---|---|---|
| *a* | 1.0 | 1.5 | 200 | 10, 20, 30, 40, 50, 60, 70, 80, 90, 100, 110, 120, 130, 140, 150, 160, 170 |
| *b* | 1.0 | 1.5 | 200 | 10, 20, 30, 40, 50, 60, 70, 80, 90, 100, 110, 120, 130, 140, 150, 160, 170 |
| *c* | 1.0 | 1.5 | 200 | 10, 20, 30, 40, 50, 60, 70, 80, 90, 100, 110, 120, 130, 140, 150, 160, 170 |
| *d* | 1.0 | 1.5 | 200 | 10, 20, 30, 40, 50, 60, 70, 80, 90, 100, 110, 120, 130, 140, 150, 160, 170 |

The dynamic damping ratio ($\lambda$) and dynamic shear modulus ($G_d$) were determined according to the hysteresis loop of the fifth vibration [18]. The dynamic stress-strain curves and the dynamic shear modulus were analyzed by taking the dynamic strain value corresponding to the fifth vibration ($N = 5$) under each level of dynamic stress. In addition, the damping ratio was analyzed using the hysteresis loop of the fifth vibration under each level of dynamic stress.

*2.4. SEM Test.* The microimages were collected by scanning electron microscope (Figure 2). The samples which reached the required *W-D* cycles number were cut into test samples with the square bottom that had the dimensions of 5 mm (side) and 10 mm (height). After the sample air drying, broke it along the height of 5 mm, blew away the surface soil particles, sprayed gold on the surface, and then put it into the vacuum chamber for vacuum pumping to obtain experimental sections. The magnified images were obtained with 1000-fold and 5000-fold.

## 3. Analysis of the Experimental Results

*3.1. Dynamic Stress-Strain Relationship of the Compacted Loess under the Effects of W-D Cycles.* The dynamic stress-strain curves of the compacted loess under different numbers of *W-D* cycles and different *W-D* cyclic paths are shown in Figure 3.

The dynamic stress of compacted loess under different *W-D* cycles increased in a hyperbolic form with the gradual dynamic strain increasing (Figure 3). The relationship curves of dynamic stress-strain were in agreement with the Hardin–Drnevich model [19].

Figure 2: Scanning electron microscope and samples.

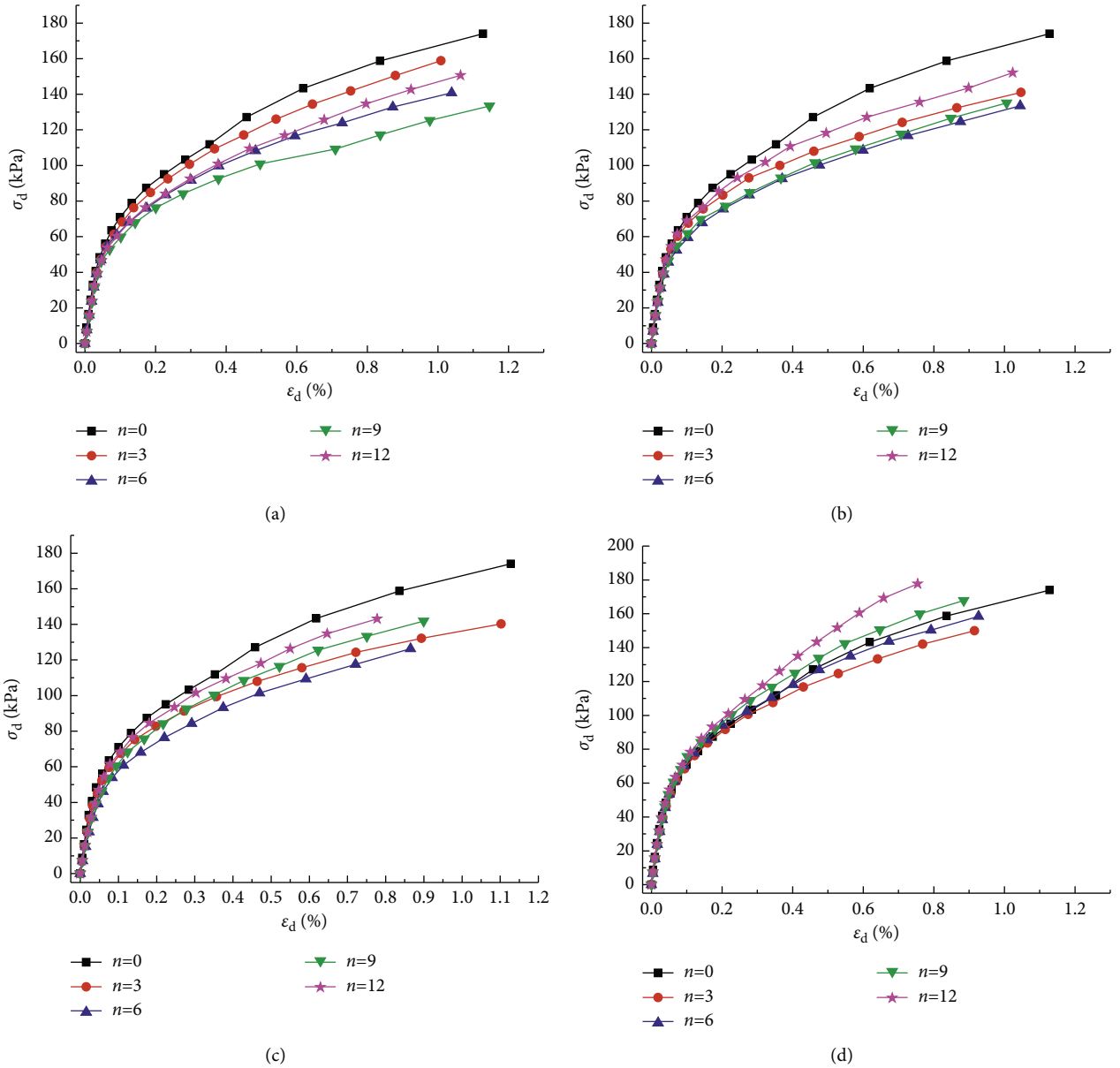


Figure 3: Dynamic stress-strain relationship of compacted loess under *W-D* cycles ($\sigma_c = 200$ kPa, $K = 1.5$, $f = 1$ Hz, and $N = 5$). (a) *W-D* cycle path *a*. (b) *W-D* cycle path *b*. (c) *W-D* cycle path *c*. (d) *W-D* cycle path *d*.

$$\sigma_{\mathrm{d}} = \frac{\varepsilon_{\mathrm{d}}}{a + b\varepsilon_{\mathrm{d}}} = \frac{\varepsilon_{\mathrm{d}}}{1/E_0 + \varepsilon_{\mathrm{d}}/\sigma_y}, \quad (1)$$

where $\sigma_d$ represents dynamic stress (kPa); $\varepsilon_d$ represents dynamic strain (%); $a$ and $b$ represent test constant; $E_0$ represents initial dynamic modulus (MPa); $\sigma_y$ represents maximum dynamic stress (kPa); and $E_0 = 1/a$, $1/\sigma_y = b$.

The dynamic stress-strain curves were obviously affected by the *W-D* cycles. The dynamic stress-strain curves of different *W-D* cyclic paths showed different characteristics with the number of *W-D* cycles increasing. The dynamic stress-strain curves of path *a* gradually moved down with the number of *W-D* cycles increasing. When $n = 9$, the dynamic stress-strain curve was located at the lowest end of the coordinate, whereas the dynamic stress-strain curve moved up when $n = 12$ (Figure 3(a)). The dynamic stress-strain curves of path *b* and path *c* were located at the lowest end when $n = 6$, and gradually moved up when $n = 9$ and $n = 12$ (Figure 3(b)). Furthermore, the amplitude of path *c* moving up was larger than that of path *b* (Figure 3(c)). The dynamic stress-strain curve of path *d* was located at the lowest end when $n = 3$. The dynamic stress-strain curve gradually moved up when $n = 6$, $n = 9$, and $n = 12$. The curve moved further up than the initial stress-strain curve ($n = 0$) when $n = 9$ and $n = 12$ (Figure 3(d)).

*3.2. Dynamic Shear Modulus of the Compacted Loess.* The dynamic shear modulus of the compacted loess was calculated by

$$G_{\mathrm{d}} = \frac{E_{\mathrm{d}}}{2(1+\mu)}, \quad (2)$$

$$\gamma_{\mathrm{d}} = \varepsilon_{\mathrm{d}}(1+\mu), \quad (3)$$

$$G_{\mathrm{d}} = \frac{\gamma_{\mathrm{d}}}{a' + b'\gamma_{\mathrm{d}}} = \frac{G_0}{1 + G_0\gamma_{\mathrm{d}}/\tau_y}, \quad (4)$$

where $E_d$ represents dynamic modulus (MPa); $G_{\mathrm{d}}$ represents dynamic shear modulus (MPa); $\gamma_d$ represents dynamic shear strain; $\mu$ represents Poisson's ratio; $a$' and $b$' represent test constant, respectively; $G_0$ represents initial dynamic shear modulus (MPa); $\tau_y$ represents maximum dynamic shear stress (kPa); and $G_0 = 1/a$', $1/\tau_{\mathrm{y}} = b$'.

The test data were transformed using equation (4), and linear fitting between the values of parameters $1/G_{\mathrm{d}}$ and $\gamma_{\mathrm{d}}$ was performed. The fitting parameters are listed in Tables 4–7, whereas the fitting curves are shown in Figure 4.

It had a good linear fitting relationship between the reciprocal of dynamic shear modulus ($G_d$) and the dynamic shear strain ($\gamma_d$), and the fitting correlation coefficients had values of more than 0.99 (Tables 4–7). The intercept and slope of the curves between $1/G_d$ and $\gamma_d$ changed with the number of *W-D* cycles increasing, whereas the variation trend was obviously influenced by the path of *W-D* cycles (Figure 4).

The initial dynamic shear modulus ($G_0$) decreased firstly and then increased gradually with the number of *W-D* cycles increasing (Figure 5). When $n = 9$, the initial dynamic shear modulus of *W-D* cyclic path *a* reached the minimum value and then increased. However, the rate of increase was relatively slow. The initial dynamic shear modulus of *W-D* cyclic path *b* and path *c* reached the minimum value at $n = 6$, after which it began to increase gradually. The initial dynamic shear modulus of *W-D* cyclic path *d* reached the minimum value at $n = 3$, after which it increased gradually, and exceeded the initial dynamic shear modulus of $n = 0$ at $n = 12$. Because of the different moisture content amplitudes of the *W-D* cycles, the initial dynamic shear modulus were obvious differences for the same *W-D* cycles number. The initial dynamic shear modulus of the different moisture content amplitude in the number of 12 *W-D* cycles were found in the following descending order: *W-D* cycle paths $c < d < b < a$.

Table 4: Fitting parameters of $G_d$ and $\gamma_d$ of *W-D* cycle path *a*.

| Fitting parameter | *W-D* cycle path *a* | | | | |
|---|---|---|---|---|---|
| | 0 | 3 | 6 | 9 | 12 |
| *a*' | 0.01465 | 0.01538 | 0.01654 | 0.01791 | 0.01773 |
| *b*' | 16.145 | 17.268 | 18.184 | 19.306 | 17.741 |
| $R^2$ | 0.9959 | 0.9957 | 0.9963 | 0.9932 | 0.9942 |

The maximum dynamic shear stress ($\tau_y$) of compacted loess was obviously affected by the *W-D* cycles number (Figure 6). The maximum dynamic shear stress of compacted loess decreased gradually and then increased with the *W-D* cycles number increasing. The variation pattern was similar to the change curve of the initial dynamic shear modulus ($G_0$) (Figure 5). When $n = 9$, the maximum dynamic shear stress of *W-D* cyclic path *a* reached the minimum value and then increased. The maximum dynamic shear stress of *W-D* cyclic paths *b* and *c* reached the minimum at $n = 6$ and then began to increase gradually. The maximum dynamic shear stress of *W-D* cycle path *d* reached the minimum value at $n = 3$, after which, it increased gradually. Because of the different water content amplitudes of the *W-D* cycles, the maximum dynamic shear stress was an obvious difference for the same *W-D* cycles number. The water content amplitude of the variation of the maximum dynamic shear stress values for 12 *W-D* cycles was found in the following descending order: W-D cycle paths $c < d < b < a$.

*3.3. Damping Ratio of the Compacted Loess under W-D Cycles.* The representative dynamic stress-strain curve was selected as the hysteretic curve (Figure 7). The hysteresis loop area represents the corresponding energy consumption. The ratio of the energy consumed by the periodic dynamic load in a cycle to the potential energy corresponding to the maximum shear strain in the cycle is the damping ratio ($\lambda$).

According to the dynamic triaxial test of compacted loess, the dynamic stress-strain time history curve was determined, and the hysteresis circle was drawn using the dynamic stress and strain of the 5th vibration. Furthermore, the damping ratio ($\lambda$) of the compacted loess was calculated using the following equation:

Table 5: Fitting parameters of $G_d$ and $\gamma_d$ of *W-D* cycle path *b*.

| Fitting parameter | *W-D* cycle path *b* | | | | |
|---|---|---|---|---|---|
| | 0 | 3 | 6 | 9 | 12 |
| *a*' | 0.01465 | 0.01563 | 0.01693 | 0.01791 | 0.016 |
| *b*' | 16.145 | 17.717 | 19.859 | 19.638 | 16.484 |
| $R^2$ | 0.9959 | 0.9962 | 0.9960 | 0.9975 | 0.9956 |

Table 6: Fitting parameters of $G_d$ and $\gamma_d$ of *W-D* cycle path *c*.

| Fitting parameter | *W-D* cycle path c | | | | |
|---|---|---|---|---|---|
| | 0 | 3 | 6 | 9 | 12 |
| *a*' | 0.01465 | 0.01644 | 0.02084 | 0.01976 | 0.01835 |
| *b*' | 16.145 | 17.681 | 18.826 | 16.882 | 15.506 |
| $R^2$ | 0.9959 | 0.9982 | 0.9981 | 0.9970 | 0.9976 |

Table 7: Fitting parameters of $G_d$ and $\gamma_d$ of *W-D* cycle path *d*.

| Fitting parameter | *W-D* cycle path *a* | | | | |
|---|---|---|---|---|---|
| | 0 | 3 | 6 | 9 | 12 |
| *a*' | 0.01465 | 0.01623 | 0.01563 | 0.01558 | 0.01384 |
| *b*' | 16.145 | 16.531 | 15.527 | 14.976 | 14.178 |
| $R^2$ | 0.9959 | 0.9980 | 0.9983 | 0.9972 | 0.9957 |

$$\lambda = \frac{1}{4\pi} \cdot \frac{A}{A_L}, \tag{5}$$

where $\lambda$ represents damping ratio; $A$ represents the area of the hysteresis loop; and $A_L$ represents the triangle OAB area (Figure 7).

The damping ratio ($\lambda$) of compacted loess samples with different *W-D* cycle paths and different *W-D* cycles numbers was calculated and fitted in semilogarithmic coordinates using equation (6). The fitting parameters are listed in Tables 8–11. The fitting curves are shown in Figure 8.

$$\lambda = m + p \cdot \lg(\varepsilon_d), \tag{6}$$

where $\lambda$ represents damping ratio; $m$ and $p$ represent fitting parameters; and $\varepsilon_d$ represents dynamic strain.

The damping ratio ($\lambda$) and dynamic strain ($\varepsilon_d$) curves fitted according to equation (6) were linear, and the fitting correlation coefficients were all more than 0.99 (Tables 8–11). The damping ratio increased linearly with the dynamic strain increasing (Figure 8). The slope of the curves changed significantly with the *W-D* cycles number increasing, and the variation pattern was obviously different due to the influence of *W-D* cycle path. When $n = 0$, the slope of the curve was the highest for *W-D* cyclic paths *a*, *b*, and *c*. The slope of the straight line decreased gradually with the *W-D* cycles number increasing. When $n = 9$, the slope of the straight line reached the minimum value for the *W-D* path *a* and then, it increased with the *W-D* cycles number increasing (Figure 8(a)). When $n = 6$, the slope of the straight line reached the minimum for *W-D* cyclic paths *b* and *c* and then increased with the *W-D* cycles number increasing (Figures 8(b) and 8(c)). When $n = 3$, the slope of the straight line reached the minimum for the *W-D* path *d* and then increased with the *W-D* cycles number increasing. The slope of the straight line at $n = 12$ was greater than that at $n = 0$ for the *W-D* path *d* (Figure 8(d)).

In order to further analyze the effect of the *W-D* cycles number on the damping ratio ($\lambda$) of each *W-D* cyclic path, the change rate ($\eta$) of the damping ratio was defined. The slope ($p$) of damping ratio ($\lambda$) and dynamic strain ($\varepsilon_d$) curve in the semilogarithmic coordinate system was used to calculate the change rate ($\eta$) of the damping ratio according to equation (7), and the relationship between the rate of change of damping ratio ($\eta$) and the *W-D* cycles number ($n$) was established (Figure 9).

$$\eta = \frac{p_0 - p_n}{p_0}, \tag{7}$$

where $\eta$ represents the change rate of the damping ratio and $p_0$ represents the slope of damping ratio ($\lambda$) and dynamic strain ($\varepsilon_d$) curve in semilogarithmic coordinate when $n = 0$. $p_n$ represents the slope of damping ratio ($\lambda$) and dynamic strain ($\varepsilon_d$) curve in the semilogarithmic coordinate when $n = 3$, 6, 9, 12.

The damping ratio ($\varepsilon_d$) of the compacted loess was obviously affected by the *W-D* cycles number. The change rate ($\eta$) of the damping ratio of compacted loess gradually increased and then decreased with the *W-D* cycles number increasing (Figure 9). Affected by the *W-D* cyclic paths, the *W-D* cycles number corresponding to the peak value of the rate of change of damping ratio was different, in which the *W-D* cyclic path *a* had $n = 9$, the *W-D* cyclic path *b* and path *c* had $n = 6$, and the *W-D* cyclic path *d* had $n = 3$. The water content amplitudes of *W-D* cycles corresponding to different

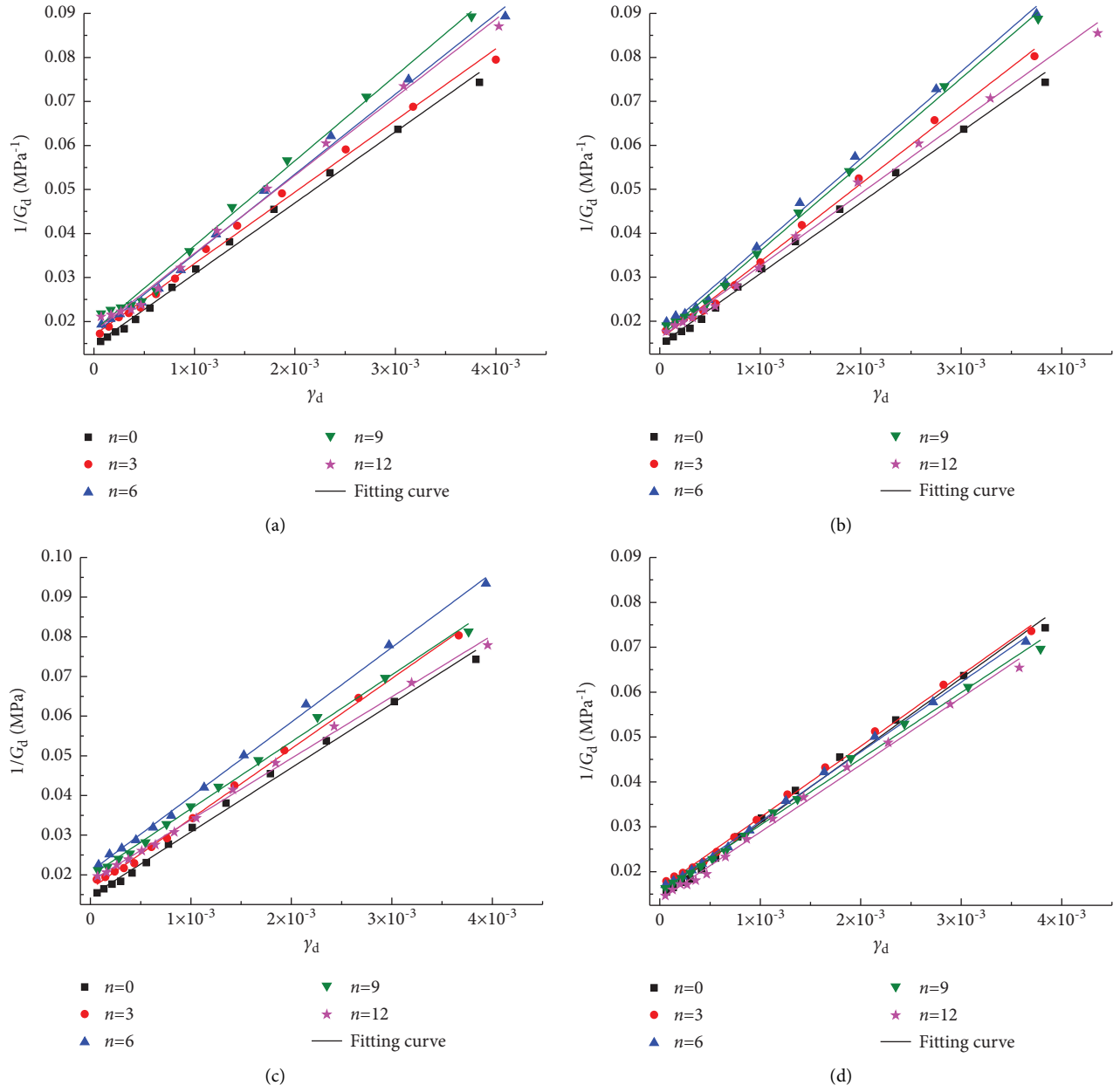


FIGURE 4: The relationship between dynamic shear modulus $G_d$ and dynamic shear strain $\gamma_d$ of compacted loess under *W-D* cycles ($\sigma_c = 200$ kPa, $K = 1.5$, $f = 1$ Hz, $N = 5$). (a) *W-D* cycle path *a*. (b) *W-D* cycle path *b*. (c) *W-D* cycle path *c*. (d) *W-D* cycle path *d*.

*W-D* cyclic paths were different. When the water content amplitude of the *W-D* cycle was larger (*W-D* cyclic path *d*), the *W-D* cycles number was smaller when the change rate ($\eta$) of the damping ratio reached the peak value. However, it was not the maximum value among the peak values for the four *W-D* cycle paths. The maximum change rate ($\eta$) of the damping ratio was for the *W-D* cycle path *c*, which indicated that there was a specific *W-D* cycle amplitude and the impact of the *W-D* cycle on the damping ratio of the compacted loess was the greatest under the condition of the *W-D* cycle water content amplitude.

## 4. Dynamic Properties Change Mechanism under the Effect of *W-D* Cycles

*4.1. Causes Analysis of Dynamic Properties Change.* The initial structure of the loess was formed after the completion of the compaction construction. In the later operation, the initial structure changed under the influence of natural and human factors, such as water and load (static and dynamic). After the repeated action of water and load (static and dynamic), the evolution of the structural characteristics of compacted loess was divided into three stages, namely the

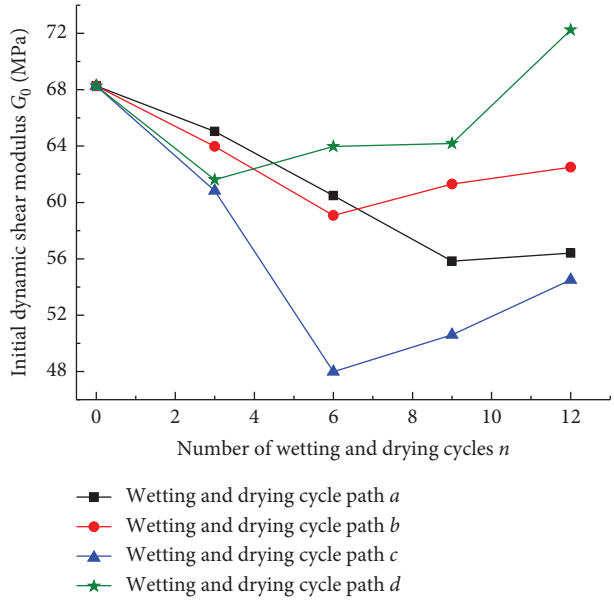


Figure 5: Relationship between $G_0$ and $n$.

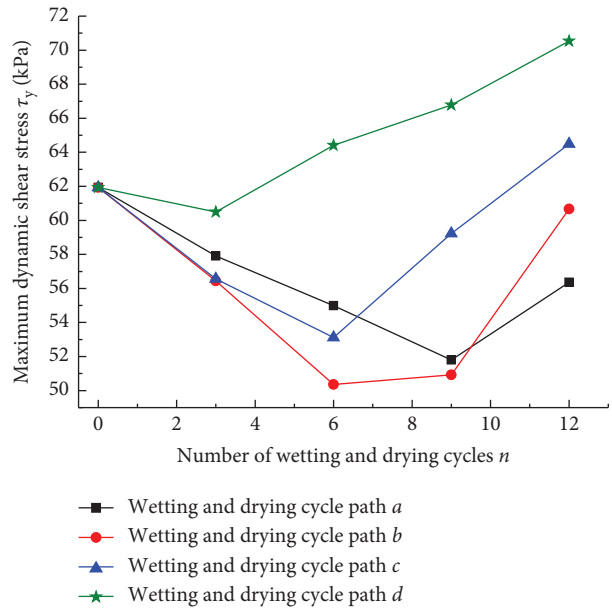


Figure 6: Relationship between $\tau_y$ and $n$.

structural damage, the structural strengthening, and the structural stability.

For the twelve *W-D* cycles, the $G_0$ and $\tau_y$ of compacted loess first decreased and then gradually increased (Figures 5 and 6). The change rate ($\eta$) of the damping ratio of the compacted loess first increased and then decreased (Figure 9). The pattern of change had an obvious turning point. The *W-D* cycle number corresponding to the turning point was called the critical *W-D* cycles number (represented by $n_c$). When $n \le n_c$, the $G_0$ and $\tau_y$ of compacted loess decreased and the change rate of damping ratio increased with the *W-D* cycles number increasing. Additionally, the soil samples showed the structure deterioration under the influence of *W-D* cycles. This represented the structure damage stage. When $n > n_c$, the $G_0$ and $\tau_y$ of the compacted loess increased and the change rate of damping ratio decreased with the *W-D* cycles number increasing. In addition, the soil samples showed structural strengthening, thus representing the structural strengthening stage. The critical *W-D* cycles number ($n_c$) corresponding to different amplitudes was different, and for the path *a*, *b*, *c*, and *d*, the corresponding values was $n_c = 9$, 6, 4.5, and 3.

In the stage of structural damage, water infiltration made the number of pores increase continuously in the soil. In the

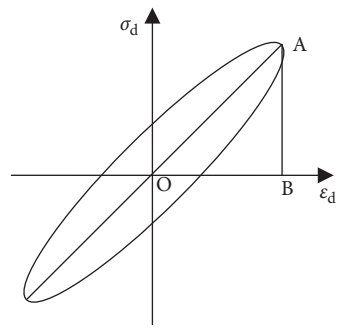


Figure 7: Dynamic stress-strain hysteresis loop.

Table 8: Fitting parameters of $\lambda$ and $\varepsilon_d$ of *W-D* cycle path *a*.

| Fitting parameter | *W-D* cycle path *a* | | | | |
|---|---|---|---|---|---|
| | 0 | 3 | 6 | 9 | 12 |
| $M$ | 0.3305 | 0.2878 | 0.2714 | 0.2408 | 0.2542 |
| $p$ | 0.0427 | 0.0359 | 0.0330 | 0.0281 | 0.0301 |
| $R^2$ | 0.9952 | 0.9987 | 0.9977 | 0.9980 | 0.9978 |

Table 9: Fitting parameters of $\lambda$ and $\varepsilon_d$ of *W-D* cycle path *b*.

| Fitting parameter | *W-D* cycle path *b* | | | | |
|---|---|---|---|---|---|
| | 0 | 3 | 6 | 9 | 12 |
| $m$ | 0.3305 | 0.2995 | 0.2502 | 0.2703 | 0.2876 |
| $p$ | 0.0427 | 0.0340 | 0.0293 | 0.0324 | 0.0351 |
| $R^2$ | 0.9952 | 0.9969 | 0.9990 | 0.9972 | 0.9992 |

Table 10: Fitting parameters of $\lambda$ and $\varepsilon_d$ of W-D cycle path *c*.

| Fitting parameter | *W-D* cycle path *c* | | | | |
|---|---|---|---|---|---|
| | 0 | 3 | 6 | 9 | 12 |
| $m$ | 0.3305 | 0.2561 | 0.2351 | 0.2732 | 0.2879 |
| $p$ | 0.0427 | 0.0306 | 0.0271 | 0.0335 | 0.0361 |
| $R^2$ | 0.9952 | 0.9975 | 0.9964 | 0.9988 | 0.9984 |

Table 11: Fitting parameters of $\lambda$ and $\varepsilon_d$ of *W-D* cycle path *d*.

| Fitting parameter | *W-D* cycle path *a* | | | | |
|---|---|---|---|---|---|
| | 0 | 3 | 6 | 9 | 12 |
| $m$ | 0.3305 | 0.2518 | 0.2733 | 0.2945 | 0.3532 |
| $p$ | 0.0427 | 0.0288 | 0.0334 | 0.0370 | 0.0467 |
| $R^2$ | 0.9952 | 0.9960 | 0.9954 | 0.9941 | 0.9932 |

process of air drying, water evaporation made cracks appear on the surface and inside of the sample, and the total porosity increase (Figure 10). The development of cracks was the main factor that led to the structural damage and the dynamic properties of compacted loess decrease. In addition, the volumetric water content of the sample decreased, and the matric suction increased. The compressive stress between the soil particles under the action of the shrinkage membrane in the capillary zone increased with the matrix suction increasing, due to which, the pore space and the void fraction of soil particles decreased [20]. In this process, the damage effect of dry shrinkage was greater than the strengthening effect of the compressive stress. When the *W-D* cycles amplitude was small (such as *W-D* cyclic path *a*), the damaging effect of the humidity and dehumidify in the soil sample was slower, and the crack development on the surface of the sample was not obvious (such as *W-D* cyclic path *a*, Figure 10). The degree of damage gradually increased with the amplitude increasing, whereas the corresponding *W-D* cycles number gradually decreased ($n = 6$ for *W-D* cycle path *b*, $n = 3$–$6$ for *W-D* cycle path *c*, and $n = 3$ for *W-D* cycle path *d*). The overall damaging effect of compacted loess

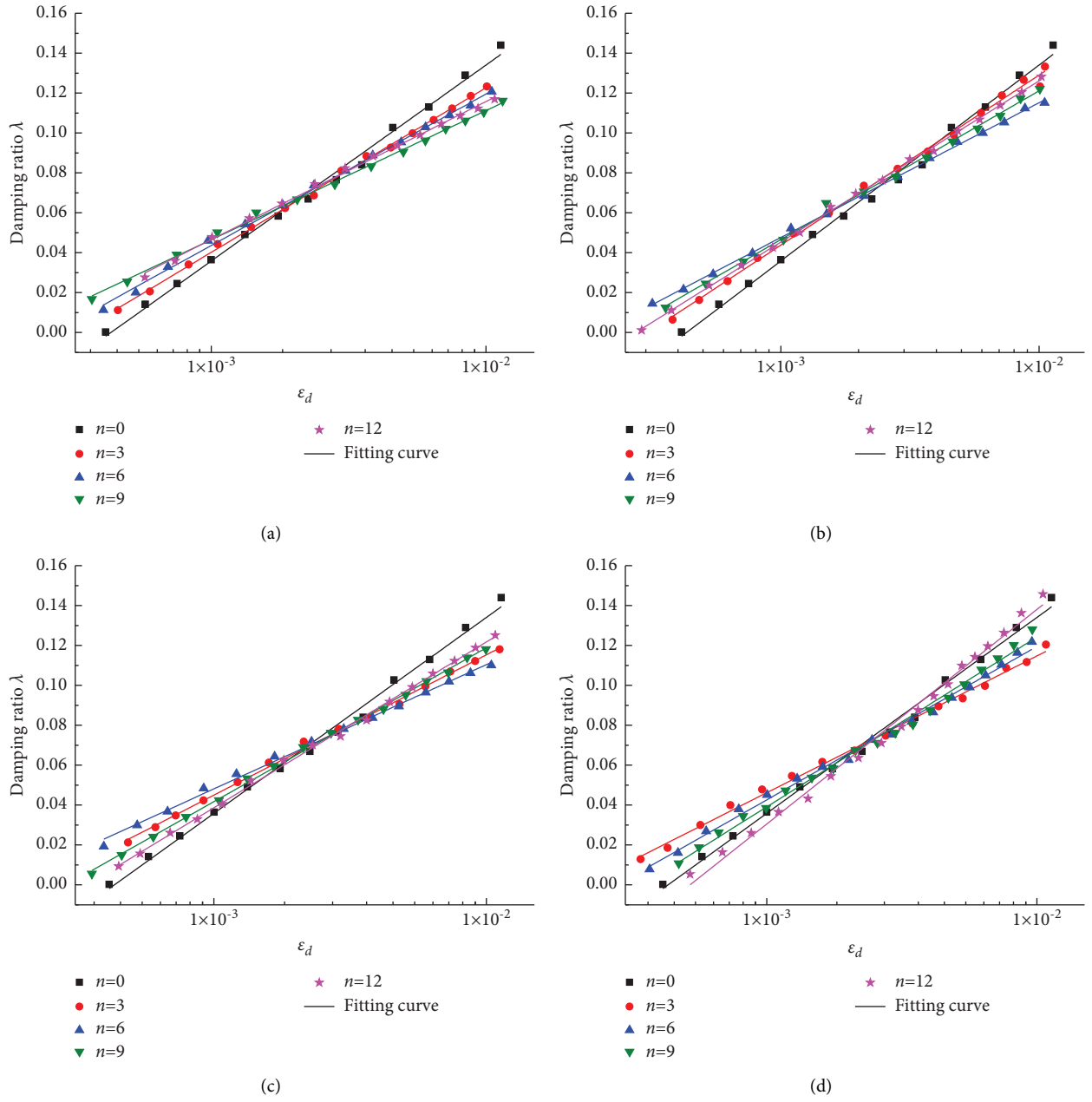


FIGURE 8: The relationship between the damping ratio $\lambda$ and dynamic strain $\varepsilon_d$ of compacted loess under W-D cycle ($\sigma_c = 200$ kPa, $K = 1.5$, $f = 1$ Hz, $N = 5$). (a) *W-D* cycle path *a*. (b) *W-D* cycle path *b*. (c) *W-D* cycle path *c*. (d) *W-D* cycle path *d*.

was greater than the enhancement effect in this stage. The $G_0$ and $\tau_y$ of soil decreased, and the change rate of the damping ratio increased.

In the stage of structural strengthening, the repeated effect of matrix suction on soil particles reduced the porosity and the void ratio. The *W-D* cycles amplitude was larger (such as *W-D* cyclic paths *b* and *c*, Figure 10), and the dry shrinkage of soil samples was more obvious. Although there were cracks in the process of dry shrinkage, the soil sample tended to be dense, as shown by the *W-D* cycle path *d* in Figure 10, which was the surface cracks feature of the sixth *W-D* cycle. Furthermore, when the *W-D* cycles number exceeded the critical *W-D* cycles number ($n_c = 3$), the development of cracks on the surface of the soil sample was relatively lower than that in the *W-D* cyclic path *d*. The enhancement effect of the structure of the soil sample was greater than the damaging effect with the *W-D* cycles number increasing. Therefore, the $G_0$ and $\tau_y$ gradually increased after reaching the minimum value corresponding to the critical *W-D* cycles number for the four *W-D* cycle paths (Figures 5 and 6). The change rate of the damping ratio decreased gradually after reaching the maximum value corresponding to the critical *W-D* cycles number for the four *W-D* cyclic paths (Figure 9).

After a certain *W-D* cycles number, the compacted loess samples were drained and consolidated before performing

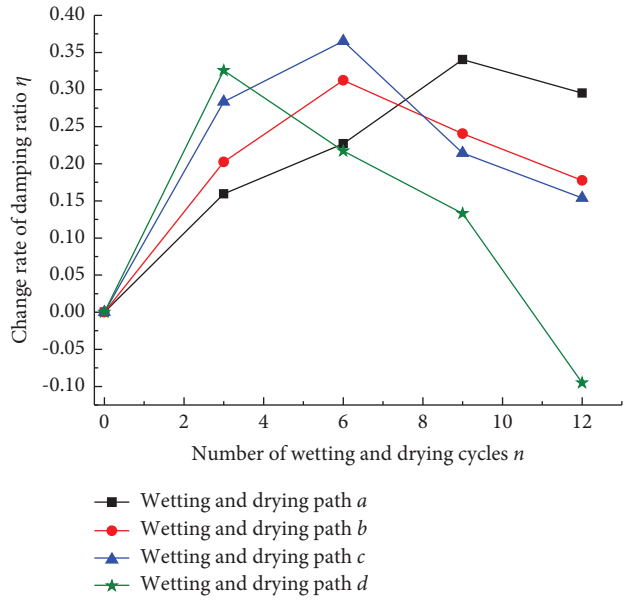


Figure 9: The relationship between $\eta$ and $n$.


Figure 10: Surface crack characteristics of samples with different cyclic paths after the 6th *W-D* cycle dehumidification.

the dynamic properties test. The relationship between the axial consolidation strain and the *W-D* cycles number was established to analyze the influence of consolidation confining pressure ($\sigma_c = 200$ kPa) on the dynamic properties. It was obvious that the axial consolidation strain of compacted loess samples did not always increase with the *W-D* cycles number increasing and showed the same variation pattern as the change of the $G_0$ and $\tau_y$ (Figure 11). There were also a critical number of *W-D* cycles ($n_c$) for axial consolidation strain, which was consistent with the critical number of *W-D* cycles for dynamic properties corresponding to different *W-D* cycle paths. The structural damage or strengthening occurred before the sample consolidation, which further verified the rationality of the above-given analysis. The consolidation confining pressure had no obvious effect on the dynamic properties of compacted loess under the *W-D* cycles.

*4.2. Evolution of the Microstructure of Compacted Loess.* The SEM images were obtained using SEM tests and are shown in Figure 12. Due to the space limitation, the SEM images of the *W-D* cyclic path *b* was only listed in this paper.

When $n = 0$, the skeleton particles of compacted loess were the aggregate particles, which were in the form of a

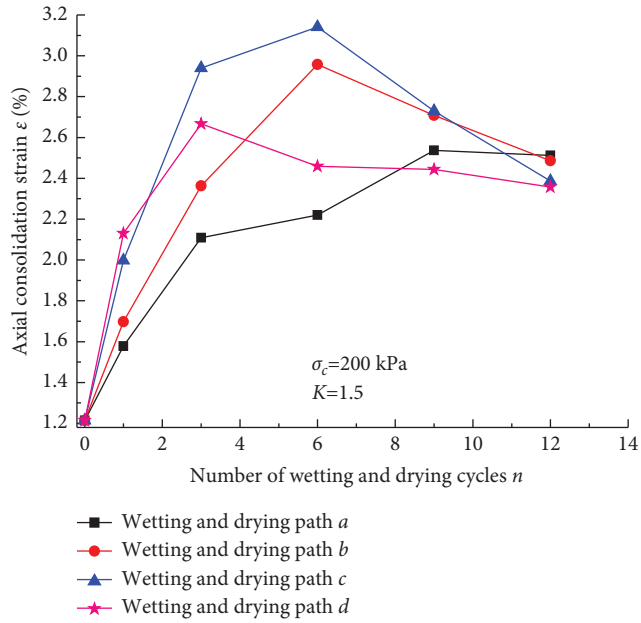


Figure 11: The axial consolidation strain of different *W-D* cyclic paths ($\sigma_c = 200$ kPa, $K = 1.5$).

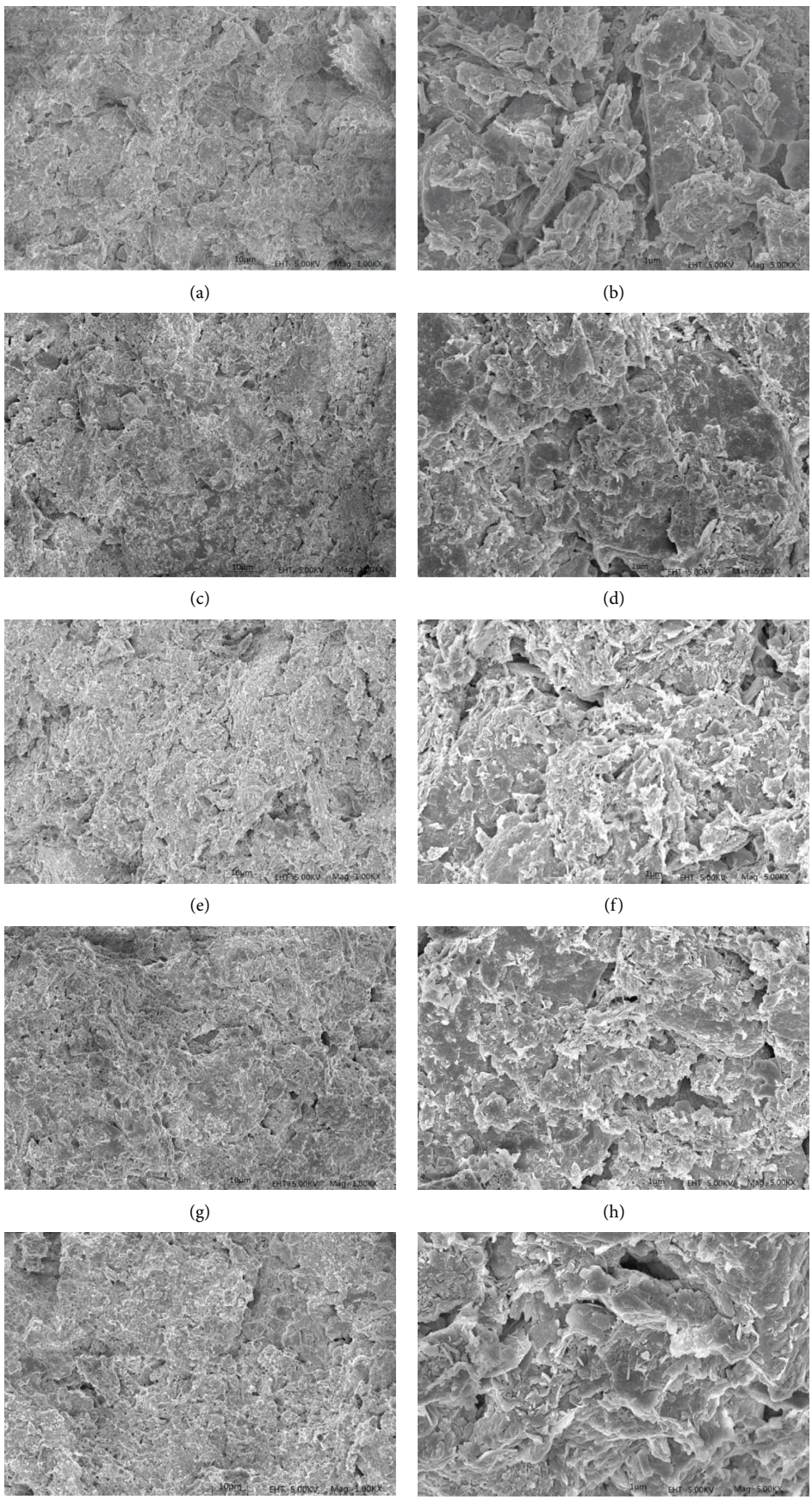

Figure 12: SEM images of *W-D* cycle path *b*. (a) $n = 0$ (1000X); (b) $n = 0$ (5000X); (c) $n = 3$ (1000X); (d) $n = 3$ (5000X); (e) $n = 6$ (1000X); (f) $n = 6$ (5000X); (g) $n = 9$ (1000X); (h) $n = 9$ (5000X); (i) $n = 12$ (1000X); (j) $n = 12$ (5000*X*).

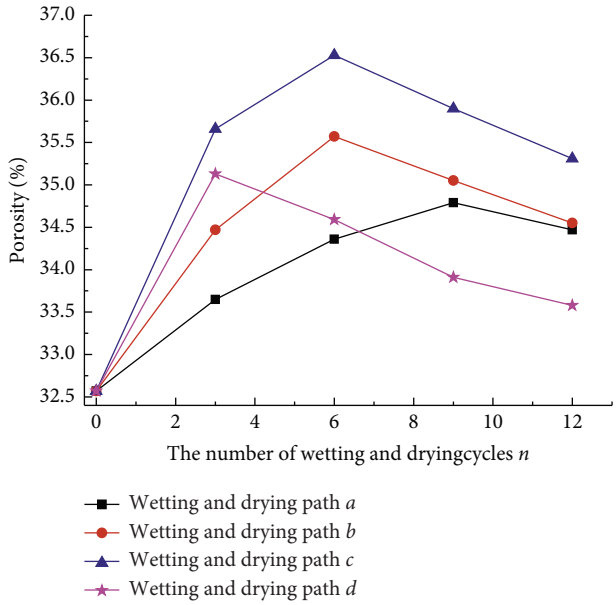


FIGURE 13: Changes of porosity of compacted loess under *W-D* cycles.

coagulum. The particles were mainly in line-surface and surface-surface mosaic contact. The pores in the soil were mainly medium and small, and the content of large pores was relatively small. The edges and corners of the compacted loess particles without *W-D* cycles were relatively obvious (Figure 12, $n = 0$). The line-surface contact and the surface-surface contact between the particles decreased with the *W-D* cycles number increasing. The pores in the compacted loess gradually evolved from large and medium pores to medium and small pores with the *W-D* cycles number increasing. When $n < n_c$, the development of microcracks in SEM images of different paths was the reason for the dynamic shear modulus, the maximum dynamic shear stress, and the damping ratio decreasing gradually during the *W-D* cycles. When $n > n_c$, the compaction of matrix suction and the filling of particles to large and medium pores and cracks which reduced the porosity and improved the cohesion and occlusion between particles, made the dynamic shear modulus, the maximum dynamic shear stress, and the damping ratio increasing.

In order to further reveal why the dynamic properties of compacted loess changed under the effect of *W-D* cycles, the SEM images with different *W-D* cycles paths and numbers, magnified by 1000 times, were quantitatively processed [21]. Three areas of the soil sample section were selected for parallel determination of microparameters to make the quantitative analysis more representatives. The threshold values of 50, 200, and 800 area pixels (50 area pixels were equivalent to $0.646\,\mu m^2$ of pore area) were selected to binarize the SEM images to obtain the porosity and pore area under the effect of *W-D* cycles.

The porosity of the compacted loess increased with the *W-D* cycles number increasing, when $n = n_c$, reached the maximum value and then decreased gradually (Figure 13). In the process of humidification, the microparticles filled the large pores between the particles, and the pores number increased in the compacted loess under the effect of water. The large and medium pores evolved to the medium and small pore continuously, which made the number of pores increase. In addition, the number of pores inside the particles increased with the erosion of the microparticles and soluble salts on the surface of the particles. The increasing of total porosity was caused by the pore number increasing. In the process of air drying, the dry shrinkage resulted in the cracks development in the sample and the porosity of the compacted loess increased. When $n > n_c$, the small particles were continuously filled in the large and medium pores, the volume of the soil decreased due to the dry shrinkage, and the porosity in the soil decreased finally.

In order to further analyze the evolution of pores in soil sample under the influence of *W-D* cycles, the pores in the compacted loess were divided into five categories according to the pixel area. These categories were the micropores, the small pores, the medium pores, and the macropores. The proportion of the pore area of five pore categories during *W-D* cycles was statistically analyzed to establish the relationship between the areas of different pore types and the *W-D* cycles number (Figure 14). The macropores in the compacted loess evolved into small and medium pores, and the small pores and micropores increased with the *W-D* cycles number increasing. Except for the increasing of macropores in path *c* at $n = 3$ and $n = 6$, the macropores of the other *W-D* cycle paths decreased gradually. The number of mesopores in *a*, *b*, *c*, and *d* increased with the *W-D* cycles number increasing, respectively, reached the maximum at $n_c$ and then gradually decreased. The numbers of small pores and micropores increased in the *W-D* cycles process. The main causes for structural damage of compacted loess were the number of pores increasing and the development of cracks and microcracks in the process of *W-D* cycles. The structure of compacted loess was strengthened by the micropores increasing and the cracks closing. Through

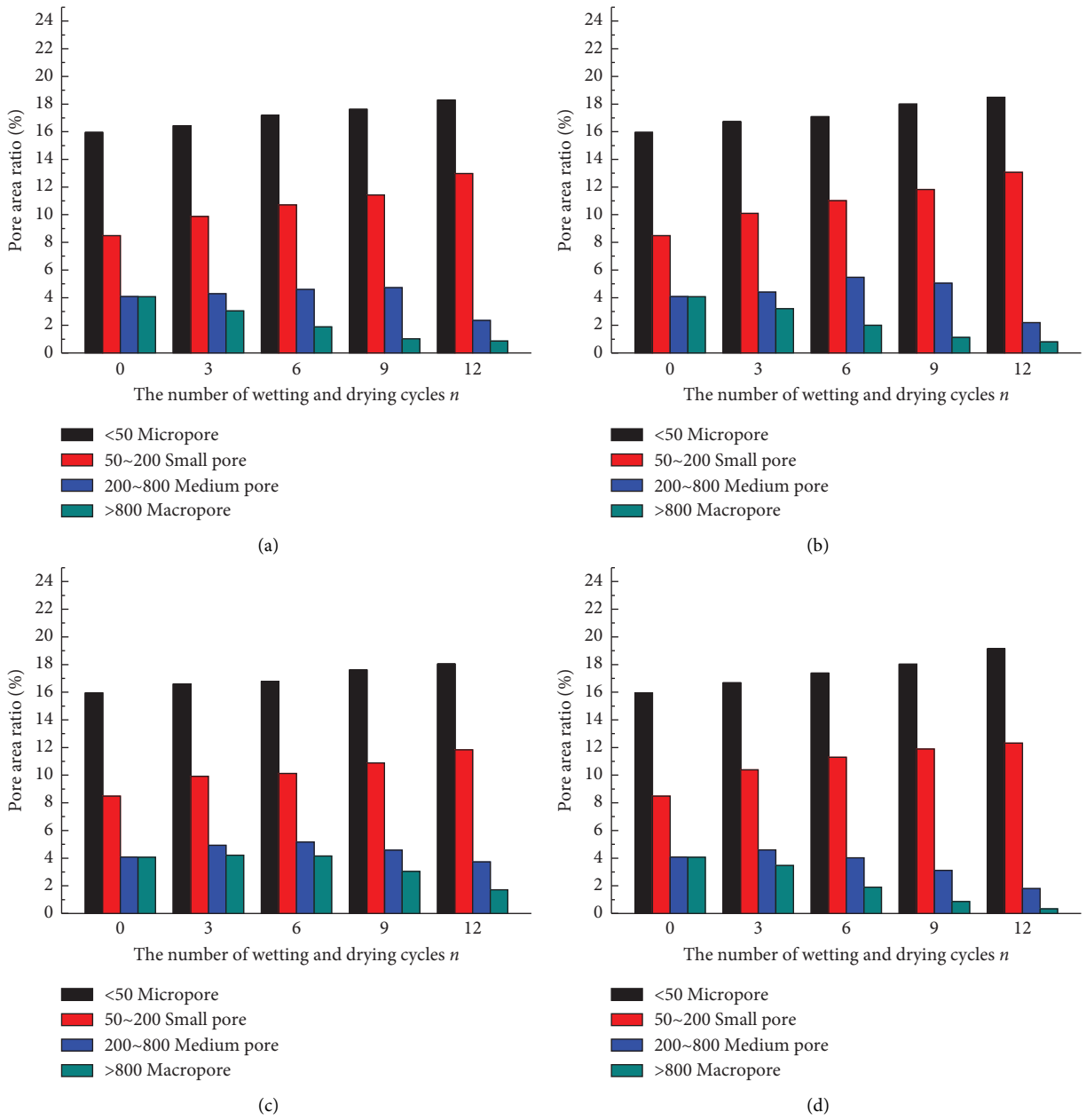


FIGURE 14: Changes of area ratio of different pore types. (a) *W-D* cycle path *a*. (b) *W-D* cycle path *b*. (c) *W-D* cycle path *c*. (d) *W-D* cycle path *d*.

comparative analysis of the pore evolution law of the four cycles, it could be concluded that the maximum damage degree of the structure was caused by the *W-D* cycle water content amplitude corresponding to the path *b* and *c*, followed by the path *a*, and the minimum was the path *d*. From the point of view of pore evolution characteristics, the micromechanism of dynamic properties changes under the *W-D* cycles was revealed.

## 5. Conclusions

Based upon the *W-D* cycle tests, soil dynamic triaxial tests, and SEM tests on the loess samples, the dynamic properties of compacted loess were systematically studied under different *W-D* cycles number. The conclusions were obtained as follows [22]:

(1) The dynamic stress-strain curves of compacted loess under *W-D* cycles conformed to the Hardin–Drnevich model. The dynamic stress-strain curves of different *W-D* cyclic paths showed different characteristics with the *W-D* cycles number increasing.

(2) The dynamic shear modulus ($G_d$) of compacted loess gradually decreased with the dynamic shear strain ($\gamma_d$) increasing. The reciprocal of the dynamic shear modulus had a good linear relationship with the dynamic shear strain. The initial dynamic shear

modulus ($G_0$) and the maximum dynamic shear stress ($\tau_y$) of the compacted loess first decreased and then gradually increased with the *W-D* cycles number increasing. Furthermore, these parameters showed different variation patterns in different *W-D* cyclic paths.

(3) The damping ratio ($\lambda$) increased with the dynamic strain ($\varepsilon_d$) increasing. The change rate ($\eta$) of the damping ratio was defined to express the variation pattern of the damping ratio under the effect of *W-D* cycles. The rate of change of the damping ratio first increased and then decreased with the *W-D* cycles number increasing.

(4) The *W-D* cycles water content amplitude affected the dynamic properties of compacted loess significantly. The critical number of *W-D* cycles was different for different amplitude, $n_c = 9$ for path *a*, $n_c = 6$ for path *b*, $n_c = 4.5$ for path *c*, $n_c = 3$ for path *d*.

(5) The main reasons for the structural damage of compacted loess were that the numbers of pores increase and cracks development on the surface and inside of the soil sample. The development of soil particle structure to mosaic structure, pore structure to uniform small pore, and matrix suction made soil sample tend to be dense, which led to structural strengthening. The evolution law of pore type revealed the micromechanism of dynamic properties under the effect of *W-D* cycles.

(6) In the actual filling project, the impact of repeated *W-D* cycles such as precipitation evaporation and groundwater level rise and fall should be considered when evaluating the dynamic properties of compacted loess. The stability of foundation, slope, and other projects was analyzed by the dynamic properties of compacted loess after *W-D* cycles.

## Abbreviations

$Q_3$: Late pleistocene epoch
$G_S$: Specific gravity of soil particle
$\rho_d$: Dry density
$W_L$: Liquid limit
$W_P$: Plastic limit
$I_p$: Plasticity index
*SEM*: Scanning electron microscope
$\sigma_d$: Dynamic stress
$\varepsilon_d$: Dynamic strain
$\alpha$ and $b$: Test constant
$E_0$: Initial dynamic modulus
$\sigma_y$: Maximum dynamic stress
$E_d$: Dynamic modulus
$G_d$: Dynamic shear modulus
$\gamma_d$: Dynamic shear strain
$\mu$: Poisson's ratio
$a$' and $b$': Test constant
$G_0$: Initial dynamic shear modulus
$\tau_y$: Maximum dynamic shear stress
$\lambda$: Damping ratio
$A$: Area of the hysteresis loop
$A_L$: Triangle OAB area
$m$ and $p$: Fitting parameters
$\eta$: Change rate of the damping ratio
$p_0$: Slope of $\lambda$-$\boldsymbol{\varepsilon_d}$ curve in semilogarithmic coordinate when $n = 0$
$p_n$: Slope of $\lambda$-$\boldsymbol{\varepsilon_d}$ curve in the semilogarithmic coordinate when $n = 3, 6, 9, 12$.

## Data Availability

All data, models generated or used during the study are included within the article. All data included in this study are available upon request to the corresponding author.

## Conflicts of Interest

The authors declare that they have no conflicts of interest.

## Acknowledgments

This study was supported by the Fund Program for Henan Bureau Group Co. Ltd of China Chemical and Geology.

## References

[1] Y. Z. Hao, T. H. Wang, and J. J. Wang, "Structural properties of unsaturated compacted loess for various sample moisture contents," *Arabian Journal of Geosciences*, vol. 12, no. 8, pp. 258–268, 2019.

[2] Y. Z. Hao, T. H. Wang, X. Jin, L. Cheng, and J. L. Li, "Experimental study on the saturated compacted loess permeability under $K_0$ consolidation," *Advances in Civil Engineering*, Article ID 1426485, 2020.

[3] Y. Z. Hao, L. Cheng, and W. F. Xiao, "Experimental study on permeability anisotropy of unsaturated compacted loess," *Advances in Civil Engineering*, Article ID 9348604, 2022.

[4] G. S. Guan, H. Rahardjo, and L. E. Choon, "Shear strength equations for unsaturated soil under drying and wetting," *Journal of Geotechnical and Geoenvironmental Engineering*, vol. 136, no. 4, pp. 594–606, 2010.

[5] L. F. Pires, O. O. S. Bacchi, and K. Reichardt, "Gamma ray computed tomography to evaluate wetting/drying soil structure changes," *Nuclear Instruments and Methods in Physics Research Section B: Beam Interactions with Materials and Atoms*, vol. 229, no. 3-4, pp. 443–456, 2005.

[6] C. S. Tang, Y. J. Cui, B. Shi, A. M. Tang, and C. Liu, "Desiccation and cracking behaviour of clay layer from slurry state under wetting-drying cycles," *Geoderma*, vol. 166, no. 1, pp. 111–118, 2011.

[7] J. Diel, H. J. Vogel, and S. Schluter, "Impact of wetting and drying cycles on soil structure dynamics," *Geoderma*, vol. 345, pp. 63–71, 2019.

[8] B. Hu, Y. Wang, B. Wang, Y. Wang, C. Liu, and C. Wang, "Impact of drying-wetting cycles on the soil aggregate stability of Alfisols in southwestern China," *Journal of Soil and Water Conservation*, vol. 73, no. 4, pp. 469–478, 2018.

[9] A. Aldaood, M. Bouasker, and M. Al-Mukhtar, "Impact of wetting–drying cycles on the microstructure and mechanical

properties of lime-stabilized gypseous soils," *Engineering Geology*, vol. 174, pp. 11–21, 2014.

[10] D. Y. Wang, C. S. Tang, Y. J. Cui, B. Shi, and J. Li, "Effects of wetting-drying cycles on soil strength profile of a silty clay in micro-penetrometer tests," *Engineering Geology*, vol. 206, pp. 60–70, 2016.

[11] C. M. Hu, Y. L. Yuan, X. Y. Wang, Y. Mei, and Z. Liu, "Comprehensive strength deterioration model of compacted loess exposed to W-D cycles," *Bulletin of Engineering Geology and the Environment*, vol. 79, no. 4, pp. 1–15, 2019.

[12] Y. Z. Hao, T. H. Wang, and Z. Wang, "Experimental study on triaxial shear characteristics of compacted loess under drying and wetting cycles," *Journal of Hydraulic Engineering*, vol. 52, no. 3, pp. 359–369, 2021.

[13] C. L. Chen, P. Yang, and J. F. He, "Research on dynamic characteristics of saturated compacted loess," *Chinese Journal of Rock and Soil Mechanics*, vol. 28, no. 8, pp. 1551–1556, 2007.

[14] W. S. Wang, G. S. Cao, Y. Li et al., "Experimental study of dynamic characteristics of tailings with different reconsolidation degrees after liquefaction," *Frontiers of Earth Science*, vol. 10, Article ID 876401, 2022.

[15] Y. M. Liu, J. D. Wang, and T. F. Gu, "Dynamic characteristics of compacted loess under cyclic loads," *Chinese Journal of Hydrogeology & Engineering*, vol. 42, no. 3, pp. 108–112, 2015.

[16] W. H. Liu, Q. Yang, and X. W. Tang, "Experimental study on the dynamic characteristics of silt clay subjected to W-D cycles under cyclic loading," *Chinese Journal of Hydraulic Engineering*, vol. 45, no. 3, pp. 261–268, 2014.

[17] T. H. Wang, Y. Z. Hao, and Z. Wang, "Experimental study on dynamic strength properties of compacted loess under wetting-drying cycles," *Chinese Journal of Rock Mechanics and Engineering*, vol. 39, no. 6, pp. 1243–1252, 2020.

[18] Standardization Administration of China (SAC), *China National Standards GB/T 50269-2015: Code for Measurement Methods of Dynamic Properties of Subsoil*, Ministry of Water Resources (2015), Beijing, China, 2015.

[19] B. O. Hardin and V. P. Drnevich, "Shear modulus and damping in soils: design equations and curves," *Journal of the Soil Mechanics and Foundations Division*, vol. 98, no. 7, pp. 667–692, 1972.

[20] Fredlund D G and H. Rahardjo, *Soil Mechanics for Unsaturated Soils*, John Wiley & Sons, New York, NY, USA, 1993.

[21] C. Liu, B. Shi, J. Zhou, and C. Tang, "Quantification and characterization of microporosity by image processing, geometric measurement and statistical methods: application on SEM images of clay materials," *Applied Clay Science*, vol. 54, no. 1, pp. 97–106, 2011.

[22] W. S. Wang, G. S. Cao, Y. Li et al., "Effects of freeze-thaw cycles on strength and wave velocity of lime-stabilized basalt fiber-reinforced loess," *Polymers*, vol. 14, no. 7, p. 1465, 2022.